sustainability

MDPI

Article

A Study on the Conditions of Fog Generation and the Change Rule of Fog Zone Length in Air Intake Roadway

Yan Wu, Hongqing Zhu *, Baozhen Zhang, Lintao Hu, Shuwei Wang and Jiuli Liu

School of Emergency Management and Safety Engineering, China University of Mining and Technology-Beijing, Beijing 100083, China; 18829029145@163.com (Y.W.); wzhangbaozhen@163.com (B.Z.); hlt_1998@163.com (L.H.); ucaswsw@163.com (S.W.); liujiuli98@163.com (J.L.)

* Correspondence: zhq@cumtb.edu.cn

Abstract: Fog in mine air intake roadways is a non-negligible disaster that seriously reduces the visibility of the roadway, affects vehicle transportation and the safe passage of personnel, and jeopardizes the safe production of the mine. This paper applies both field testing and numerical simulation to explore fog formation conditions and the effects of inlet air temperature and humidity on the fog zone length within the Wangjialing Mine's air intake roadway in Shanxi, China. First, based on the consideration of the relationship between the moisture gain of surrounding rock and the temperature with humidity of the air flow, the fog generation and distribution law model of the air intake roadway was established. Based on this model, the critical inlet air temperature and the critical inlet air relative humidity for fogging in the Wangjialing Mine air intake roadway were determined. In addition, we found that the fogging point inside the roadway shifted forward continuously with the increase in inlet air temperature and inlet air relative humidity, and the length of the fog zone expands parabolically in response to these rising conditions.

Keywords: fog generation; mine air intake roadway; air relative humidity; air temperature

Citation: Wu, Y.; Zhu, H.; Zhang, B.; Hu, L.; Wang, S.; Liu, J. A Study on the Conditions of Fog Generation and the Change Rule of Fog Zone Length in Air Intake Roadway. *Sustainability* **2024**, *16*, 4192. https://doi.org/10.3390/su16104192

Academic Editor: Sanjay Nimbalkar

Received: 4 April 2024
Revised: 7 May 2024
Accepted: 8 May 2024
Published: 16 May 2024

1. Introduction

Fog represents a natural occurrence, characterized by minute water droplets or ice crystals floating in the air just above the ground, arising from the condensation of water vapor in the lower atmospheric layer. The presence of these droplets within the atmosphere markedly diminishes visibility when fog forms [1–5]. This phenomenon is commonly seen in mines located within subarctic and tropical regions [6], Notably, certain mines in China also experience artificially induced fog [7–9]. From June to August each year, the main air intake roadway of the Wangjialing mine in Shanxi Province suffers from severe fog hazards which cause low visibility inside the roadway, seriously affecting the safety of mine personnel and vehicle traffic [10–16]. In addition, foggy environments can reduce the productivity of mine personnel in their work, and allow pollutants to remain in the air for long periods of time, which can be detrimental to the health of mine personnel [17–19].

Fog formation is closely related to changes in surrounding temperature and humidity [20–26]. It is important to study the pattern of temperature and humidity changes in the roadway in order to study the formation of fog. Xihua Zhou et al. [27] measured and analyzed data from the Dongtan mine excavation roadway, proposing an equation describing the relationship between air flow and heat exchange with surrounding rock in the roadway, and the changes in the heat transfer circle. Jianliang Gao et al. [28] investigated the heat and moisture exchange process between the air flow and the surrounding rock in the presence of moisture evaporation at the wall, discovering that five parameters, namely the wall moisture coefficient, rock thermo-physical properties, roadway size, convective heat exchange coefficient, and ventilation time, significantly impact changes in air flow temperature and humidity in the roadway. Yijiang Wang et al. [29] researched the non-stationary heat transfer mechanism of moist surrounding rocks and found that latent heat

transfer resulting from moisture diffusion has a crucial effect on the thermal environment of the mine. Dechao Deng [30] used the empirical formula of Sherbani and the Lewis relation to determine heat and mass transfer coefficients and established a mathematical model of heat and moisture exchange between the air flow and the wall of the excavation face. Pingye Guo et al. [31] discovered that the roughness of the surrounding rock increases the effective heat transfer coefficient between the surrounding rock and the air flow, thereby enhancing the heat transfer between them. These studies have focused on the effects of mine ventilation and air flow temperature and humidity on each other; however, there are no studies that show how these factors affect fog formation.

Many scholars have also studied the causes and characteristics of mine fog. Zenghua Li [32] found that when the air pressure in the tunnel is suddenly lowered, the air suddenly expands, and at this time, it is easier for fog to form. Martikainen et al. [33,34] presented three Finnish fogging mines, where data on humidity and temperature inside the mines were measured, and it was found that the fogging zones were correlated with the difference between the air temperature and the dew point temperature. Chuanle Yang et al. [35] analyzed the causes of fog in the upper mountain of Gaozhuang coal mine, and proposed that it should be considered from the perspective of the ventilation system, so as to achieve the purpose of eliminating the fog; Xueqian Qi et al. [36] measured the parameters of the wet air at the fogging of the acid prickly gully coal mine, and the results showed that the fogging was mainly related to the humidity of the roadway, the temperature, the change in the roadway topography, and the leakage of the roadway air. Shenghua Zou et al. [37] investigated the relationship between particle size distribution and environmental parameters such as wind speed, temperature, and relative humidity during the formation of fog in coal mine roadways. Xiaofeng Zhi et al. [38] established a flow field and fog distribution model for an open pit coal mine, and studied the flow field distribution in the mine under different fan combinations. Xiaodong Wang et al. [39] analyzed the influencing factors of fog formation in the return air shaft section of a mine and calculated the amount of temperature, humidity, airflow, and other factors on fog formation.

Although the causes and characteristics of fog in mines have been investigated both in China and abroad, the effect of inlet air on the fog zone of the roadway has not been thoroughly examined. Therefore, this paper discusses the effects of the inlet air relative humidity and the inlet air temperature on the fogging point and the length of the fog zone in the inlet air. We conducted on-site measurements of air flow temperature, air flow relative humidity, surrounding rock temperature and wind speed in the mine air intake roadway. Subsequently, an equation for the relationship between moisture gain and relative humidity versus temperature was developed based on the source of moisture dissipation in the air intake roadway and applied to a newly developed numerical model to replicate the field tests. Finally, the model was applied to assess the conditions of fog generation in the air intake roadway, as well as to evaluate how variations in inlet air relative humidity and inlet air temperature influence the pattern of fog zone length. The findings from these studies will provide the basis for subsequent defogging of the air intake roadway and contribute to the sustainable development of the mine.

2. Field Test

2.1. Test Preparation

The test was conducted in an air intake roadway at the Wangjialing mine in Shanxi, China, with a total length of 12.8 km. Notably, the 0–3 km section is a straight, uphill section, where the fog often starts to form. In order to exclude the influence of other factors, this study mainly concentrates on examining the area within 3 km of the air intake roadway. The roadway is domed, with a cross-sectional area of about 20 m^2 and a hydraulic diameter of 4.5 m, a height of 4.1 m, and a width of 5.2 m, as shown in Figure 1. Mine personnel and vehicles enter the underground through the roadway.

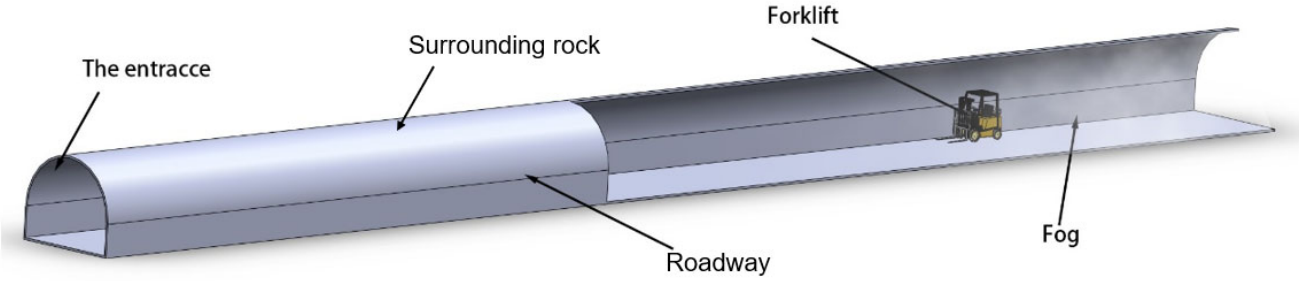

Figure 1. Schematic diagram of the roadway.

Within 3 km of the air intake roadway, one measurement point was arranged every 0.2 km to test the air flow temperature, surrounding rock temperature, air flow relative humidity, and wind speed, as shown in Figure 2. The temperature and relative humidity are measured by the YWSD 50/100 mine intrinsically safe temperature and humidity detector (Jining, China), the surrounding rock temperature is measured by the CWH600 mine infrared thermometer (Jinan, China), and the wind speed is measured by the JFY-4 ventilation multi-parameter detector (Xuzhou, China), and the specific parameters of the equipment are shown in Table 1. All measurement points will be measured three times and the average of the three measurements will be taken as the final result, where both sides of the wall are measured when measuring the surrounding rock temperature, three measurements are taken on each side, and the final result is the average of the six measurements.

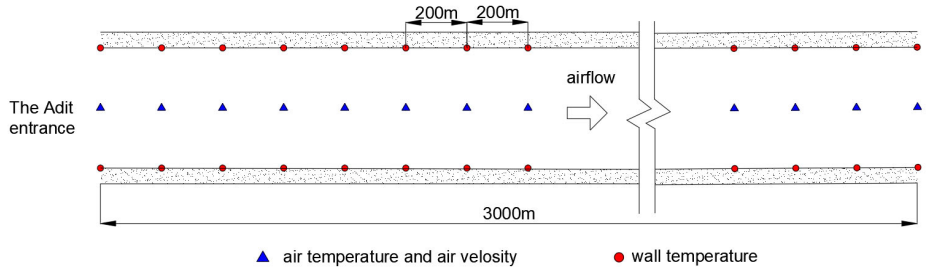

Figure 2. Measurement point layout.

Table 1. Specific parameters of the measurement equipment.

Equipment	Measured Parameters	Range	Resolution	Accuracy
YWSD50/100 mine intrinsically safe temperature and humidity detector	airflow temperature	−30~100 °C	0.01 °C	±0.5 °C
	airflow relative humidity	0%~100%	0.01%	±0.5%
Mine Infrared Thermometer CWH600	surrounding rock temperature	−30~600 °C	0.1 °C	±2%
JFY-4 ventilation multi-parameter detector	wind speed	0.2~20 m/s	0.1 m/s	0.2~5 m/s: 0.1 m/s; 5~20 m/s: ±0.25 m/s

2.2. Test Results

According to the results of the field tests, the natural wind direction is from the outside to the roadway, and the wind speed inside the roadway is stabilized at about 2.5 m/s. The fog is distributed within 1.5–3 km from the entrance of the roadway. The fog was distributed within 1.5–3 km from the entrance of the roadway, as shown in Figure 3. As the roadway is part of a mine, only explosion-proof cameras could be carried to take photographs, and the dim conditions of the roadway made it difficult for the explosion-proof camera to capture the fog in a very noticeable way. In fact, the concentration of fog was much worse than shown in the photographs, with visibility of less than 50 m in extreme cases.

Figure 3. Field test situation: (**a**) roadway with no fog; (**b**) roadway with fog.

Figure 4 shows the distribution of air flow and surrounding rock temperatures in the air intake roadway. The air flow temperature remains slightly higher than the surrounding rock temperature. Both temperatures exhibit a similar trend, initially experiencing a rapid decrease followed by a more gradual decline. This is due to the fact that the temperature at the roadway entrance is mainly influenced by the conditions within the mountain's interior. With increasing distance from the roadway entrance, the surrounding rock temperatures and air flow temperatures are less influenced by the external environment and more influenced by the interior of the mountain. On the other hand, the decreasing trend of air flow temperature at 1.5 km abruptly decelerates, and the temperature disparity widens notably beyond this point. This suggests that fog begins to form at 1.5 km, and the heat released during condensation counteracts the cooling of the airflow. This finding aligns with the observed distribution of fog in the field.

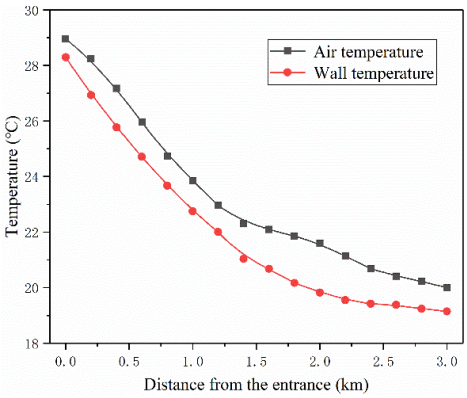

Figure 4. Test results of air flow temperature and surrounding rock temperature along the roadway.

Figure 5 shows the variation in air flow temperature and air flow relative humidity in the air intake roadway. It can be found that the air flow relative humidity increases rapidly and then reaches the maximum value at 1.5 km, while the air flow temperature has been decreasing throughout the process. The increase in the relative humidity of the air flow is attributed to the decrease in the temperature of the air flow and, concurrently, to the persistent evaporation of moisture from the surrounding environment. The field study revealed noticeable moisture on the surface of the surrounding rock and on the ground, as shown in Figure 6.

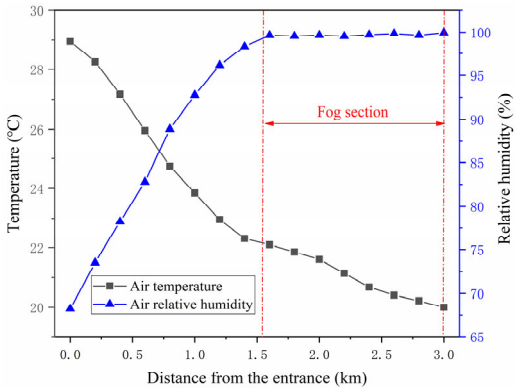

Figure 5. Test results of air flow temperature and relative humidity along the roadway.

Figure 6. Moisture source: (**a**) damp ground; (**b**) damp walls.

According to the basic principle of fog generation, when the air is saturated and the temperature continues to drop, the moisture in the air will precipitate out and form fog. Field test results indicate that upon entering the roadway, the airflow's relative humidity began a steady ascent. At 1.5 km from the entrance of the air intake roadway, the relative humidity of the air flow reached more than 99%, which was saturated, and then the relative humidity of the air flow remained in the saturated state. Meanwhile, the temperature of the air flow in the air intake roadway consistently dropped, culminating in fog formation in the zone extending from 1.5 to 3 km from the tunnel's entrance.

3. Numerical Simulation

A model of fog generation and distribution law in the air intake roadway was established, and the numerical model was used to study the effects of inlet air relative humidity and inlet air temperature on the generation and distribution of fog in the air intake roadway. Because Ansys Fluent has a strong function for simulating the material transport and heat transfer process, it is widely used in the thermal analysis of mixtures; therefore, it is used in this study.

3.1. Governing Equations

The heat and moisture exchange between the mine surrounding rock and the wind flow is very complicated, and the following assumptions are made to facilitate the study:

(1) The air flow is a one-dimensional steady flow in the axial direction.
(2) The air flow is a constant, incompressible fluid.
(3) Do not count the water vapor condensation and heat dissipation.
(4) Mass force is not counted.
(5) The surrounding rock is isotropic and homogeneous in all directions, and the thermophysical parameters are constant.

In this study, component transport and energy models were enabled to simulate the variation in water vapor mass fraction in the air flow. The standard k-ε model is used to calculate thermal interactions, and the component transport model is commonly used to represent changes in humidity in the air, and it is widely used in tunnel ventilation and heat and moisture transfer simulations [40,41].

The governing equations for the solution of the current problem can be expressed as follows in Equations (1)–(7) [42–44]. These equations will be solved using Ansys Fluent 2017, a computational fluid dynamics software.

Continuity equation:

$$\frac{\partial u_i}{\partial x_i} = 0 \tag{1}$$

Momentum equation:

$$\frac{\partial \rho u_i}{\partial t} + \frac{\partial \rho u_i u_j}{\partial x_j} = -\frac{\partial p}{\partial x_i} + \frac{\partial}{\partial x_j}\left[\mu\left(\frac{\partial u_i}{\partial x_j} + \frac{\partial u_j}{\partial x_i}\right)\right] + \frac{\partial\left(-\rho u_i u_j\right)}{\partial x_j} \tag{2}$$

Energy equation:

$$\frac{\partial(\rho E)}{\partial t} + \frac{\partial(u_i(\rho E + p))}{\partial x_i} = \frac{\partial}{\partial x_i}\left(k_{eff}\frac{\partial T}{\partial x_i}\right) - \sum_{j'} h_{j'} J_{j'} + u_j\left(\tau_{ij}\right)_{eff} + S_h \tag{3}$$

Component transport equation:

$$\frac{\partial}{\partial t}\rho Y_i + \nabla \cdot \rho \vec{v} Y_i = -\nabla \cdot \vec{J}_i + R_i + S_i \tag{4}$$

k equation:

$$\frac{\partial k}{\partial t} + u_j \frac{\partial k}{\partial x_j} = \frac{1}{\rho}\frac{\partial}{\partial x_j}\left[\left(\mu + \frac{\mu_t}{\sigma_k}\right)\frac{\partial k}{\partial x_j}\right] + \frac{\mu_t}{\rho}\left(\frac{\partial u_i}{\partial x_j} + \frac{\partial u_j}{\partial x_i}\right)\frac{\partial u_i}{\partial x_j} - \varepsilon \tag{5}$$

ε equation:

$$\frac{\partial \varepsilon}{\partial t} + u_j \frac{\partial \varepsilon}{\partial x_j} = \frac{1}{\rho}\frac{\partial}{\partial x_j}\left[\left(\mu + \frac{\mu_t}{\sigma_\varepsilon}\right)\frac{\partial \varepsilon}{\partial x_j}\right] + \frac{C_1 \mu_t}{\rho}\frac{\varepsilon}{k}\left(\frac{\partial u_i}{\partial x_j} + \frac{\partial u_j}{\partial x_i}\right)\frac{\partial u_i}{\partial x_j} - C_2\frac{\varepsilon^2}{k} \tag{6}$$

Turbulent viscosity μ_t:

$$\mu_t = C_\mu \rho k^2/\varepsilon \tag{7}$$

where u_i is the air velocity; μ_t and μ are the molecular and turbulent viscosities, respectively; k and ε are the turbulent kinetic energy and the molecular dissipation rate, respectively; S_h is the volumetric heat source; S_i is the rate of production of the added dispersed phase plus a user-defined source term; R_i is the net rate of production of component i by chemical reaction; and $\vec{J}_i$ is the diffusive flux of the component. x_i, x_j are the distances in the i-direction, j-direction, ρ is the density, C_1, C_2, C_μ, σ_k, σ_ε are constants set to default values, $C_1 = 1.44$, $C_2 = 1.92$, $C_\mu = 0.09$, $\sigma_k = 1.0$, $\sigma_\varepsilon = 1.3$.

The initial conditions are

$$u(t = 0) = u_0,\ T(t = 0) = t_0$$

3.2. The Model and Boundary Conditions

In this paper, a simplified model of the air intake roadway is developed with a length of 3 km and a hydraulic diameter of 4.5 m, as shown in Figure 7. The finite volume method was adopted and solved using Fluent solver. The solution equations include the energy equation, standard k-ε model, and component transport model. According to the selection

of boundary conditions and solution equations, the parameters that need to be given in the simulation process include air flow velocity, inlet airflow temperature, surrounding rock temperature, inlet air relative humidity, surrounding rock moisture dissipation, and roughness height. The spatial coordinate system is selected, and the cross-section Z = 0 is set as the inlet of the model velocity flow, and the cross-section Z = L is the free outlet of the model, where L is the length of the roadway. The velocity of the inlet air flow is 2.5 m/s, the temperature is 28.95 °C, and the relative humidity is 68.23%. The pressure stabilization basis, the steady state model, and the SIMPLE algorithm were selected, and the component gas mixture was set to be a mixture of water vapor and air in wet air, and the residuals of each monitoring were uniformly controlled at the level of 10^{-6}, and were calculated separately after initialization. After the residuals converge, the temperature and relative humidity data of each node are output.

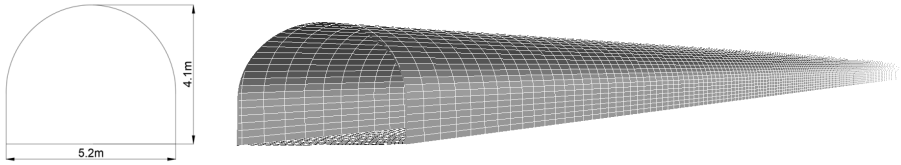

Figure 7. Model schematic.

The surrounding rock temperature and longitudinal depth were fitted as shown in Figure 8, and the distribution of the surrounding rock temperature was applied to the wall boundary conditions by means of the udf custom function. Furthermore, the moisture gain of the internal environment of the air intake roadway was introduced as a source term.

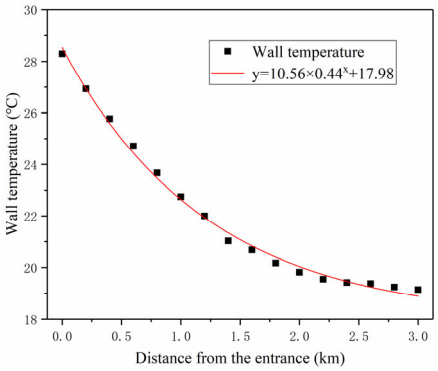

Figure 8. Surrounding rock temperature fitting curve.

3.3. Identification of Source Terms

Moisture on the ground and on the walls of the enclosure can easily evaporate into the air, resulting in a faster increase in the relative humidity of the air intake roadway. It is therefore essential to discuss the magnitude of moisture gain on the ground and on the walls of the enclosure. For a thin layer of water on the surface of the enclosure, when the thickness of the water layer on the ground is less than 1 mm, the moisture gain can be calculated according to the following formula:

$$w = \alpha(z_b - z_a)\frac{101,325}{B}\beta \tag{8}$$

where w is the amount of moisture gain, g/h m^2; B is the actual atmospheric pressure of the project, Pa; z_b is the absolute humidity of the saturated air corresponding to the wet bulb temperature of the project, g/m^3; z_a is the absolute humidity of the wet air in the project, g/m^3, and can be taken as the product of the absolute and relative humidity of the saturated state corresponding to the dry bulb temperature; α is related to the ventilation

and waterproofing measures in the mine roadway, and is taken as 1/3 in this paper; β is the moisture exchange coefficient, m/h.

The moisture exchange coefficient β can be calculated from Equations (9)–(13).

$$\beta = \frac{0.66D}{L}\left(\frac{gL^2}{v^2} \times \frac{\rho_b - \rho}{\rho_b} \times P_r\right)^{0.26} \tag{9}$$

where g is the acceleration of gravity, 9.8 m/s^2; L is the characteristic size, m; P_r is the Brownian coefficient, $P_r = 0.61$; D is the diffusion coefficient, m^2/n; v is the viscous coefficient of motion corresponding to T_p, m^2/s; ρ, ρ_b are the density of the air, the density of the air in the point of saturation state, respectively.

$$D = 0.0754\frac{T_p}{273.15} \times \frac{101,325}{B} \tag{10}$$

where T_p is the average of the dry and wet bulb temperatures of the air, K; 0.0754 is the diffusion constant of the air at standard conditions.

$$\rho_b = 1.293\frac{273.15}{T_{sh}}\left(1 - \frac{0.378P_{cb}}{B}\right) \tag{11}$$

$$\rho = 1.293\frac{273.15}{T}\left(1 - \frac{0.378P_{cn}}{B}\right) \tag{12}$$

where T, T_{sh} are the dry and wet bulb absolute temperature of indoor air, K; P_{cb} is the evaporated water temperature of saturated water vapor partial pressure, with no water temperature data; P_{cn} is the water vapor partial pressure of air, Pa.

According to Antoine's equation, the relationship between saturated water vapor partial pressure and temperature can be obtained as:

$$\lg P_b = a - \frac{b}{t + c} \tag{13}$$

where P_b is the saturated water vapor partial pressure, Pa; t is the air temperature, °C; a, b, and c are Antoine's constants, which can be obtained from the database of the Chinese Academy of Sciences according to the query.

The absolute humidity of the air at different temperatures can be calculated by Formulas (13) and (14).

$$z = \frac{0.622 \times P_b \times \varphi}{B - \varphi \times P_b} \tag{14}$$

where z is the absolute humidity of the air, kg/m^3; φ is the relative humidity.

The value of moisture gain at different temperatures and relative humidities can be obtained by bringing the moisture exchange coefficient and absolute humidity into Equation (8). Fitting the moisture gain to the temperature and relative humidity, the correlation between the actual moisture gain and the relative humidity as well as the temperature can be obtained, as shown in Figure 9, with the relationship equation as follows.

$$\begin{aligned} w' = {} & 1473.90 - 4298.01\varphi - 10.99T + 2762.81\varphi^2 + 31.63\varphi T + 0.02T^2 \\ & + 344.83\varphi^3 - 21.35\varphi^2 T - 0.06\varphi T^2 + 10.32\varphi^4 - 1.24\varphi^3 T + 0.04\varphi^2 T^2 \end{aligned} \quad \left(R^2 = 0.99998\right) \tag{15}$$

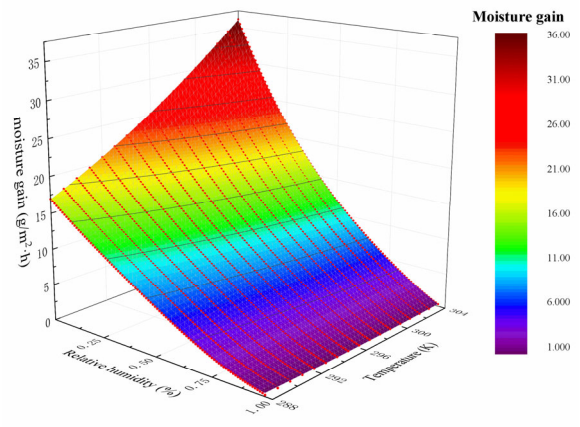

Figure 9. Correlation of moisture gain with temperature and relative humidity.

4. Fog Generation and Distribution

In this section, we first evaluate the accuracy of the numerical model, and then use the model to analyze the conditions for fog generation in the air intake roadway and the effects of different inlet air relative humidity and inlet air temperature on the length of the fog zone. Given that the temperature inside the air intake roadway is consistently decreasing, moisture in the air condenses into fog upon reaching saturation., Therefore, regions where the airflow's relative humidity surpasses 99% are considered the fog distribution area.

4.1. Model Validation

In order to verify the reliability of the numerical simulation calculations, the results of the numerical simulation were compared with the data obtained from the field test, as shown in Figure 10. The inlet air temperature was 28.95 °C and the inlet air relative humidity was 68.23%.

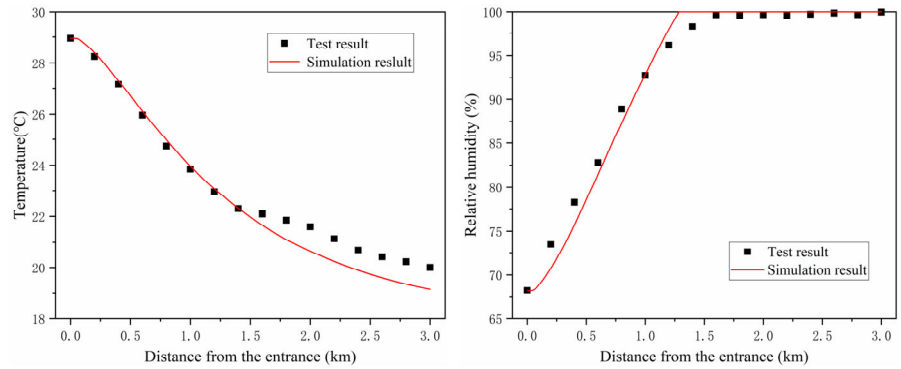

Figure 10. Comparison of simulation results and test result along the roadway: (**a**) air flow temperature along the roadway; (**b**) air flow relative humidity along the roadway.

Figure 10a displays a comparison of simulated and measured air flow temperature and relative humidity along the depth of the roadway. The figure illustrates that the simulated results closely align with the measured data, showing a cooling trend in the air flow upon entering the roadway and reaching a minimum temperature at 3 km. Particularly in the 0–1.5 km interval, there is a strong agreement between the simulation results and the measured data. In the interval of 1.5–3 km, the simulated results are slightly larger than the measured values, which is caused by the heat dissipation of water vapor condensation during the formation of fog in this zone, and the error will not affect the conclusions of this paper because the main purpose of the numerical simulation is to investigate the formation and distribution of fog. Figure 10b shows that the simulated and measured values of relative humidity in the air intake roadway are in good agreement with the measured

values. In addition, the values of air flow temperature and relative humidity at 0.2 km intervals in the numerical simulation were extracted, totaling 16 nodes, and we carried out correlation analysis with the field test data to obtain the correlation coefficients between the field test temperature and the numerical simulation temperature as 0.9960, R^2 = 0.9920, and the correlation coefficients between the field test relative humidity and the numerical simulation relative humidity as 0.9967, R^2 = 0.9933. In conclusion, the simulated values of air flow temperature and relative humidity are consistent with the measured results, which proves that the model can be used to analyze the effects of relative humidity and temperature on the formation and distribution of fog in the air intake roadway.

Figure 11 shows a cloud plot of air flow temperature versus relative humidity of the air flow across the cross-section of the air intake roadway in the direction of the depth of the roadway, from which it can be seen that the temperature of the air flow decreases and the relative humidity increases as the depth of the roadway continues to increase. The lowest air flow temperatures are located in the cross-section near the walls. After a distance of 1.5 km, the relative humidity in the cross-section is 100%.

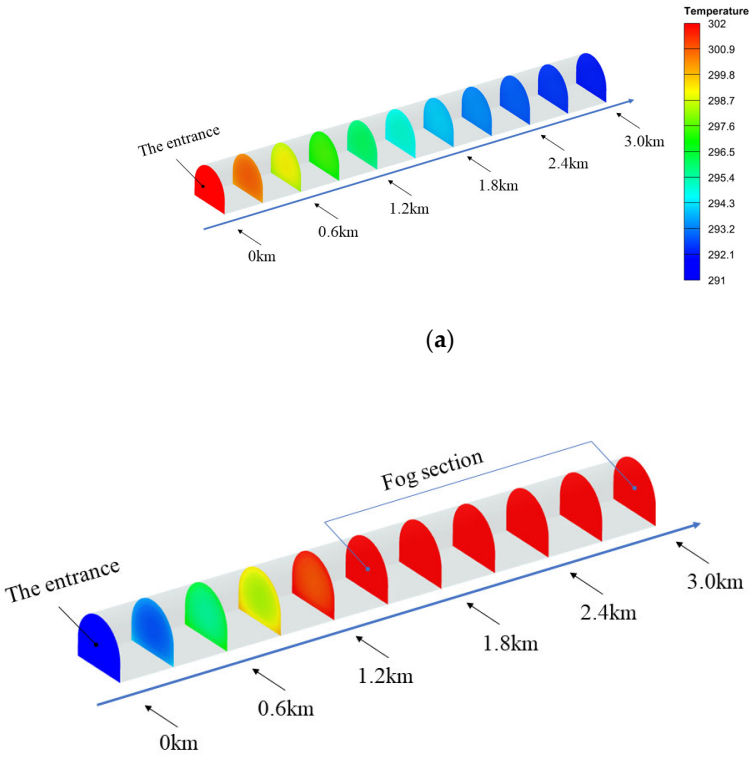

Figure 11. Air temperature and air relative humidity contours along the roadway: (**a**) air flow temperature; (**b**) air flow relative humidity.

4.2. Effect of Inlet Air Relative Humidity

In this section, the relative humidity of various inlet air flows between 52% and 81% were investigated, where the temperature of the inlet air flow was field-tested at 28.95 °C. The temperature distributions at the wall were based on the fitted results for the field-tested case, as shown in Figure 8.

Figure 12 shows the variation in the temperature as well as the relative humidity for a variety of different inlet air relative humidity conditions. It can be seen from Figure 12a that the air flow temperature decreases with the increase in the longitudinal depth, and the variation in the temperature is consistent for different relative humidity conditions. This is because the variation in air flow temperature mainly depends on the heat transfer between

the air and surrounding rock temperature, and the relative humidity of the air flow has little effect on it. As can be seen from Figure 12b, the relative humidity continues to increase with increasing longitudinal depth, eventually leading to air saturation. The variation in inlet air relative humidity has a significant effect on the relative humidity of the air flow in the roadway. A lower inlet air relative humidity makes it increasingly challenging for the air flow to attain saturation, resulting in a reduced fogging section. This suggests that reducing the inlet air relative humidity can effectively mitigate fog formation within the roadway. When the air flow relative humidity is 52.44%, the fog is no longer generated in the roadway, which means that 52.44% is the critical temperature for judging whether the air intake roadway is fogged or not under the condition of this air intake air temperature.

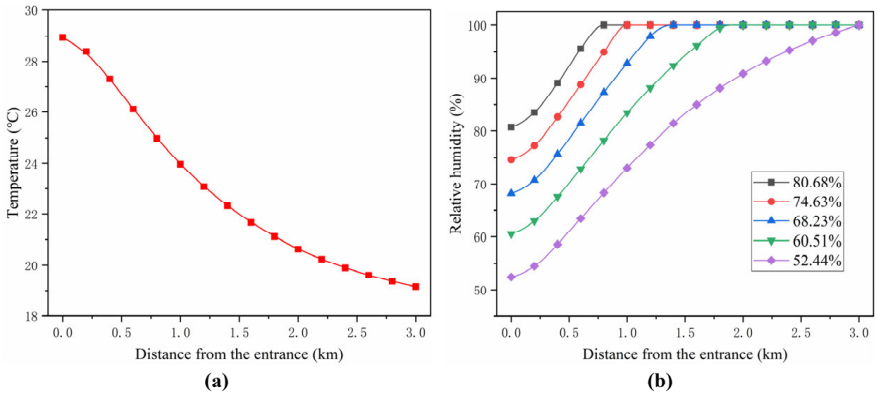

Figure 12. Variation in temperature and relative humidity along the roadway under different inlet air relative humidity: (**a**) air flow temperature; (**b**) air flow relative humidity.

As can be seen from Figures 13 and 14, the fogging point in the air intake roadway is moving forward and the length of the fog zone increases significantly as the inlet air temperature increases, and when the inlet air relative humidity is less than 52.4%, fog is no longer generated. When the inlet humidity is greater than 52.4%, the length of the fog zone increases parabolically with the increase in relative humidity. This indicates that when the inlet air relative humidity is greater than 52.4%, the lower the inlet air relative humidity, the greater its effect on the fog zone range. In the case of relatively low inlet air relative humidity, reducing the inlet air relative humidity has a better effect on alleviating the fog in the roadway.

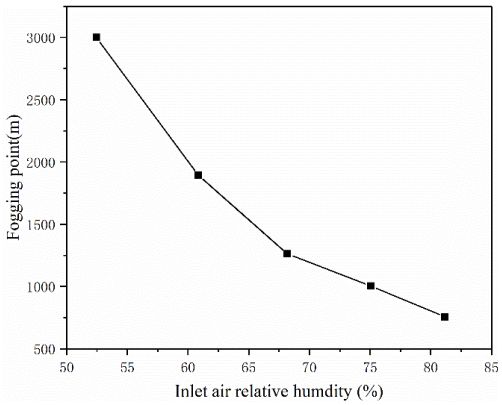

Figure 13. Fogging points under different inlet air relative humidity conditions.

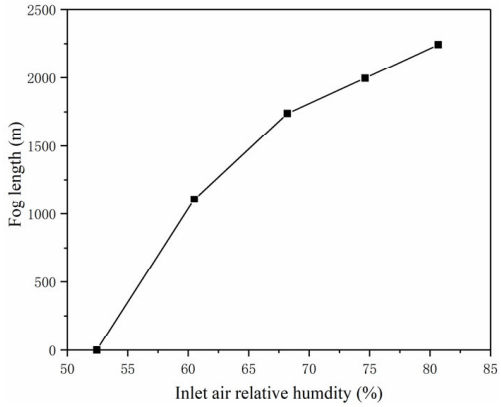

Figure 14. Length affected by fog under different inlet air relative humidity conditions.

4.3. Effect of Inlet Air Temperature

In this section, the effects of seven different inlet air temperatures between 24 °C and 30 °C on the distribution of fog formation are discussed for an inlet air humidity of 68.23%. It should be noted that the change in the temperature of the air flow not only affects the properties of the air flow itself, but also affects the surrounding rock temperature. Therefore, when the temperature of the inlet air flow changes, the distribution of surrounding rock temperature also changes at the same time.

The temperature of the rock within the mountain interior is relatively insulated from external environmental influences. However, as the proximity to the exterior increases, the rock temperature becomes more susceptible to ground environmental conditions. Consequently, it is reasonable to assume that the temperature of the surrounding rock at an infinite distance from the roadway remains constant. Furthermore, it is postulated that the temperature of the surrounding rock at the entrance of the roadway is approximately 98% of the temperature of the airflow. Based on the variation relationship of surrounding rock temperature with depth, the distribution of surrounding rock temperature at different inlet air temperatures can be obtained, as shown in Figure 15.

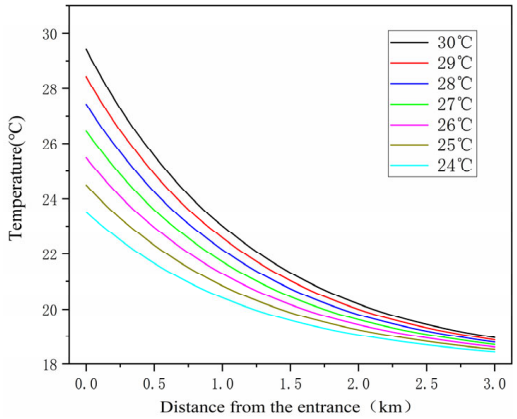

Figure 15. Variation in surrounding rock temperature along the roadway under different inlet air temperatures.

Figure 16a shows the variation in air flow temperature at different inlet air temperatures. It can be observed that, regardless of the inlet air temperature, the airflow temperature exhibits a consistent pattern of decreasing and then stabilizing. Additionally, the disparity in air flow temperature narrows as the longitudinal depth increases. This is due to the fact that after a long period of heat exchange with the surrounding rock, the air flow temperature will constantly tend to the surrounding rock temperature, while the surrounding rock temperature inside the mountain is relatively constant. Figure 16b shows the variation in air flow humidity under different inlet air temperatures. It can be seen

from the figure that the air flow humidity rises rapidly with the increase in the longitudinal depth, and finally reaches saturation. The data also reveal that lower inlet air temperatures slow the increase in air flow humidity, making it more difficult to achieve saturation and resulting in a shorter fogging section. This suggests that reducing the inlet air temperature can be an effective strategy to mitigate fogging within the air inlet refuge. When the air intake air temperature was 24 °C, the air intake roadway was no longer fogged, indicating that 24 °C is the critical temperature for determining whether the air intake roadway is fogged or not.

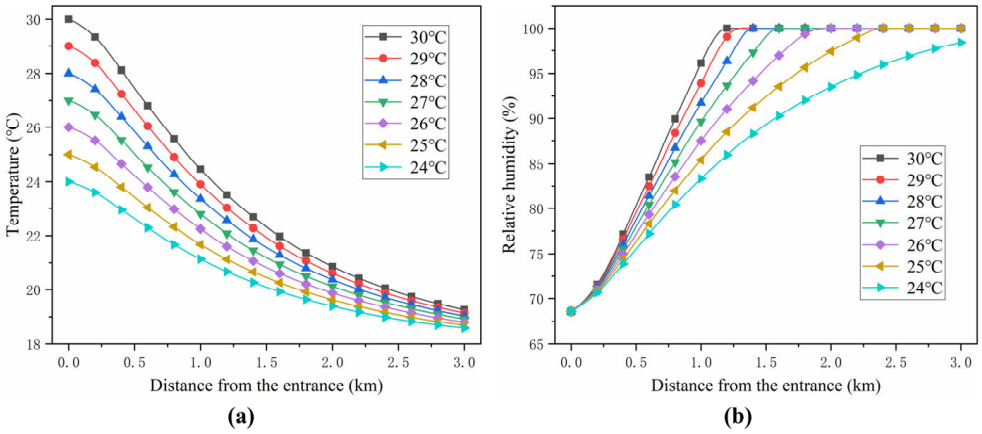

Figure 16. Variation in temperature and relative humidity along the roadway under different inlet air temperatures: (**a**) air flow temperature; (**b**) air flow relative humidity.

As can be seen from Figures 17 and 18, with the increase in inlet air temperature, the fogging point in the air intake roadway is moving forward, and the length of the fog zone increases significantly. However, when the inlet air temperature is lower than 24 °C, the air intake roadway will no longer produce fog. When the inlet air temperature is greater than 24 °C, the length of the fog zone increases parabolically with the increase in relative humidity. This indicates that when the air intake temperature is greater than 24 °C, the lower the air intake temperature, the greater the effect on the fog zone range, and lowering the air intake temperature has a better effect on alleviating the fog in the roadway when the air intake temperature is relatively low.

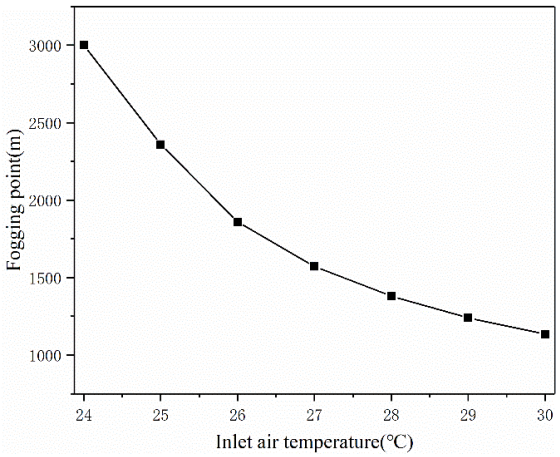

Figure 17. Fogging points under different inlet air temperature conditions.

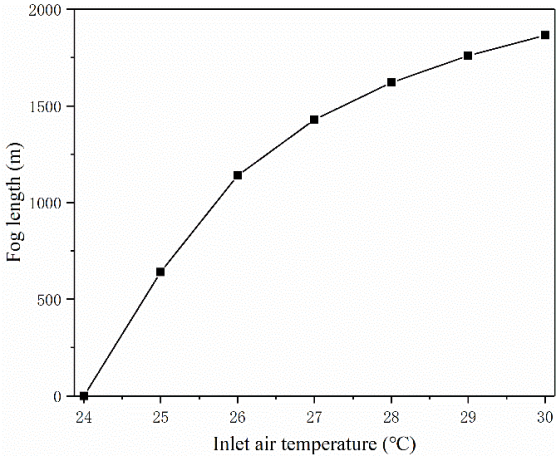

Figure 18. Length affected by fog under different inlet air temperature conditions.

5. Conclusions

In this study, air flow temperatures, surrounding rock temperatures, relative humidity of the air flow, air velocity, and fog conditions were tested in the field inside the mine air intake roadway. The field tests were reproduced by a Fluent model based on the dispersion of moisture in the surrounding rock of the air intake roadway. The numerical results were then compared with the field results to verify the accuracy of the numerical method. Furthermore, the model was used to analyze the conditions of fog generation in the air intake roadway and the effects of inlet air relative humidity and inlet air temperature on the length of the fog zone. The main conclusions drawn from this study are as follows:

(1) A model of the fog generation and distribution law in the air intake roadway was established, and the correlation between the moisture gain of surrounding rock and the relative humidity and temperature was established, which was applied in the numerical model. The accuracy of this numerical modeling approach was substantiated through a comparison of the simulated outcomes with actual field measurements, confirming the method's validity in predicting fog behavior within the roadway environment.

(2) When the inlet air relative humidity is 68.23%, the critical inlet air temperature for determining whether the air intake roadway is fogged is 24 °C. When the inlet air temperature is 28.95 °C, the critical inlet air relative humidity to determine whether fogging occurs in the roadway is 52.44%. When the inlet air relative humidity or inlet air temperature exceeds the critical point, fogging will occur in the air intake roadway.

(3) Once the inlet air relative humidity and inlet air temperature exceeded the critical point, the fog point moved forward with the increase in inlet air relative humidity and inlet air temperature. Moreover, the length of the fog zone increased parabolically with the increase in inlet air relative humidity and inlet air temperature. This observation suggests that reducing the inlet air relative humidity and inlet air temperature would yield more effective fog prevention, particularly when these parameters are maintained at lower levels.

Author Contributions: Formal analysis, writing—original draft, Y.W.; Formal analysis and supervision, H.Z.; software and field investigation, B.Z.; supervision and validation, L.H.; Data curation, S.W.; field investigation, J.L. All authors have read and agreed to the published version of the manuscript.

Funding: This research received no external funding.

Data Availability Statement: Data are contained within the article.

Conflicts of Interest: The authors declare no conflicts of interest.

References

1. Zhang, J.; Xue, H.; Deng, Z.; Ma, N.; Zhao, C.; Zhang, Q. A comparison of the parameterization schemes of fog visibility using the in-situ measurements in the North China Plain. *Atmos. Environ.* **2014**, *92*, 44–50. [CrossRef]
2. Song, J.I.; Yum, S.S.; Gultepe, I.; Chang, K.-H.; Kim, B.-G. Development of a new visibility parameterization based on the measurement of fog microphysics at a mountain site in Korea. *Atmos. Res.* **2019**, *229*, 115–126. [CrossRef]
3. Guijo-Rubio, D.; Gutiérrez, P.A.; Casanova-Mateo, C.; Sanz-Justo, J.; Salcedo-Sanz, S.; Hervás-Martínez, C. Prediction of low-visibility events due to fog using ordinal classification. *Atmos. Res.* **2018**, *214*, 64–73. [CrossRef]
4. Laskar, S.; Bhowmik, S.R.; Sinha, V. Some statistical characteristics of occurrence of fog over Patna airport. *Mausam* **2013**, *64*, 345–350. [CrossRef]
5. Achtemeier, G.L. Effects of moisture released during forest burning on fog formation and implications for visibility. *J. Appl. Meteorol. Climatol.* **2008**, *47*, 1287–1296. [CrossRef]
6. Martikainen, A. *Fog Removal in the Declines of Underground Mines in Sub-Arctic Regions*; Helsinki University of Technology: Espoo, Finland, 2007.
7. Qin, X.; Sun, J. Analysis of the causes of underground fog in Dongrong Second Mine. *Saf. Coal Mines* **2005**, *7*, 37–39.
8. Qingwen, Y.; Yongxing, L.; Haonan, F.; Xiaodong, W.; Mengjiao, J. Experimental Research on the Defogging Efficiency of Wellhead in a Lead-zinc Mine. *Min. Res. Dev.* **2021**, *41*, 168–174.
9. Mengjiao, J.; Xiaodong, W.; Haonan, F.; Shupeng, C.; Xuelin, T. Research on the Generating Mechanism and Treatment of Fog in the Return Air Wellhead of a Metal Mine. *Saf. Environ. Eng.* **2023**, *30*, 44–52+60.
10. Yang, C.; Kim, J. Road risk assessment based on road freezing and fog data. *J. Digit. Contents Soc.* **2021**, *22*, 801–807. [CrossRef]
11. Fotios, S.; Cheal, C.; Fox, S.; Uttley, J. The effect of fog on detection of driving hazards after dark. *Light. Res. Technol.* **2018**, *50*, 1024–1044. [CrossRef]
12. Belaroussi, R.; Gruyer, D. Convergence of a Traffic Signs-based Fog Density Model. In Proceedings of the 18th IEEE International Conference on Intelligent Transportation Systems, Gran Canaria, Spain, 15–18 September 2015; pp. 783–787.
13. Bullough, J.D.; Rea, M.S. Impacts of Fog Characteristics, Forward Illumination, and Warning Beacon Intensity Distribution on Roadway Hazard Visibility. *Sci. World J.* **2016**, *2016*, 4687816. [CrossRef] [PubMed]
14. Mueller, A.S.; Trick, L.M. Driving in fog: The effects of driving experience and visibility on speed compensation and hazard avoidance. *Accid. Anal. Prev.* **2012**, *48*, 472–479. [CrossRef] [PubMed]
15. Gao, J.J.; Tian, H.; Li, A.X.; Song, J.Y.; Zhu, X.X. Analysis of Agglomerate Fog Meteorological Characteristics in Anhui Province Based on Traffic Accident Data. *Pure Appl. Geophys.* **2023**, *180*, 313–333. [CrossRef]
16. Jiang, Y.; Zhang, N.; Li, A.X.; Wu, H.; Li, R.C.; Yang, J. Effects of Weather on Highway Traffic Capacity in China: Characteristics and Causes of Roadblocks Due to Fog Events. *Pure Appl. Geophys.* **2020**, *177*, 5027–5040. [CrossRef]
17. Yao, W.; Zheng, Z.; Zhao, J.; Wang, X.; Wang, Y.; Li, X.; Fu, J. The factor analysis of fog and haze under the coupling of multiple factors -- taking four Chinese cities as an example. *Energy Policy* **2020**, *137*, 111138. [CrossRef]
18. Smith, D.K.; Dorling, S.R.; Renfrew, I.A.; Ross, A.N.; Poku, C. Fog trends in India: Relationships to fog type and western disturbances. *Int. J. Climatol.* **2023**, *43*, 818–836. [CrossRef]
19. Pérez-Díaz, J.L.; Ivanov, O.; Peshev, Z.; Álvarez-Valenzuela, M.A.; Valiente-Blanco, I.; Evgenieva, T.; Dreischuh, T.; Gueorguiev, O.; Todorov, P.V.; Vaseashta, A. Fogs: Physical basis, characteristic properties, and impacts on the environment and human health. *Water* **2017**, *9*, 807. [CrossRef]
20. Ding, Y.H.; Liu, Y.J. Analysis of long-term variations of fog and haze in China in recent 50 years and their relations with atmospheric humidity. *Sci. China-Earth Sci.* **2014**, *57*, 36–46. [CrossRef]
21. Liu, T.T.; Han, Y.; Jiang, W.H. Distribution Characters of Fog in Chongqing and Causes of Fog in November 7, 2006. In Proceedings of the 2nd International Conference on Energy and Environmental Protection (ICEEP 2013), Guilin, China, 19–21 April 2013; pp. 1297–1300.
22. Dev, K.; Nebuloni, R.; Capsoni, C. Fog Prediction Based on Meteorological Variables-An Empirical Approach. In Proceedings of the International Conference on Broadband Communications for Next Generation Networks and Multimedia Applications (CoBCom), Graz, Austria, 14–16 September 2016.
23. Ye, H.C. The influence of air temperature and atmospheric circulation on winter fog frequency over Northern Eurasia. *Int. J. Climatol.* **2009**, *29*, 729–734. [CrossRef]
24. Gajananda, K.; Dutta, H.N.; Lagun, V.E. An episode of coastal advection fog over East Antarctica. *Curr. Sci.* **2007**, *93*, 654–659.
25. Yang, L.; Liu, J.W.; Ren, Z.P.; Xie, S.P.; Zhang, S.P.; Gao, S.H. Atmospheric Conditions for Advection-Radiation Fog Over the Western Yellow Sea. *J. Geophys. Res.-Atmos.* **2018**, *123*, 5455–5468. [CrossRef]
26. Izett, J.G.; van de Wiel, B.J.H. Why Does Fog Deepen? An Analytical Perspective. *Atmosphere* **2020**, *11*, 865. [CrossRef]
27. Zhou, X.; Dan, Y.; Wang, J. The Unsteady Thermal Exchange between Wall Rock and Airflow of Roadway. *J. Liaoning Tech. Univ. (Nat. Sci.)* **2002**, *21*, 264–266.
28. Gao, J.; Yang, M. Analysis of the Factors lnfluencing Temperature Distribution of Surrounding Rock and Cooled Zone Radius. *China Saf. Sci. J.* **2005**, *15*, 76–79.
29. Wang, Y.J.; Zhou, G.Q.; Wu, L. Unsteady heat-moisture transfer of wet airway in deep mining. *J. Cent. South Univ.* **2013**, *20*, 1971–1977. [CrossRef]

30. Deng, D. Numerical Study on Thermal and Humid Environment Change Rule of Excavation Face. Master's Thesis, Liaoning Technical University, Fuxin, China, 2017.
31. Guo, P.Y.; Su, Y.; Pang, D.Y.; Wang, Y.W.; Guo, Z.B. Numerical study on heat transfer between airflow and surrounding rock with two major ventilation models in deep coal mine. *Arab. J. Geosci.* **2020**, *13*, 756. [CrossRef]
32. Li, Z.; Zhang, B. Cause Analysis on Undefined Fog in Xinzhuang Coal Mine. *China Saf. Sci. J.* **2003**, *7*, 77–79+83.
33. Martikainen, A.L. Comparative evaluation of fogging phenomenon in the ramp of three mines in Finland. In Proceedings of the 8th International Mine Ventilation Congress, Brisbane, Australia, 6–8 July 2005; Citeseer: Princeton, NJ, USA, 2005; pp. 6–8.
34. Martikaninen, A. Fog mesh as an alternative fog removal method in mine ramps. *Trans.-Soc. Min. Metall. Explor. Inc.* **2007**, *320*, 38.
35. Yang, C.; He, Q. Research on the Causes and Solution Measures of Upper Mountain Fog in Gaozhuang Coal Mine. *Energy Technol. Manag.* **2005**, *1*, 34–35.
36. Qi, X.; Li, C. Study on the causes and solutions of the fog in the Suancigou coal. *Miner. Eng. Res.* **2011**, *26*, 70–74.
37. Zou, S.-H.; Li, K.-Q.; Han, Q.-Y.; Yu, C.W. Numerical simulation of the dynamic formation process of fog-haze and smog in transport tunnels of a hot mine. *Indoor Built Environ.* **2017**, *26*, 1062–1069. [CrossRef]
38. Zhi, X.; Ju, X.; Zhang, Z.; Miu, W.; Du, Y.; Zhang, Y.; Yang, X.; Cheng, H. Analysis of Fog Distribution and Defogging Effect of Opencast Coal Mine in Winter. *Sci. Technol. Ind.* **2021**, *21*, 315–320.
39. Wang, X.; Fu, H.; Liu, J.; Tong, X.; Chen, S. Analysis of the factors affecting the fog in the return air wellhead of a mine in Yunnan and research on the treatment plan. *Nonferrous Met. (Min. Sect.)* **2021**, *73*, 147–152.
40. Wei, Y.; Hu, H.; He, F.; Li, J. Numerical simulation study on heat and moisture exchange law between roadway walls and air. *China Saf. Sci. J.* **2012**, *22*, 42–47.
41. Wang, F.; Wang, M.N.; Carvel, R.; Wang, Y. Numerical study on fire smoke movement and control in curved road tunnels. *Tunn. Undergr. Space Technol.* **2017**, *67*, 1–7. [CrossRef]
42. ANSYS. *Fluent Theory Guide*; ANSYS: Canonsburg, PA, USA, 2013.
43. Li, Z.J.; Xu, Y.; Li, R.R.; Jia, M.T.; Wang, Q.L.; Chen, Y.; Cai, R.Z.; Han, Z.Q. Impact of the water evaporation on the heat and moisture transfer in a high-temperature underground roadway. *Case Stud. Therm. Eng.* **2021**, *28*, 101551. [CrossRef]
44. Liu, Y.; Liu, S.B.; Zhang, H.D. Numerical Simulation of Heat and Moisture Transfer in Deep Air Buried. In Proceedings of the 10th International Symposium on Heating, Ventilation and Air Conditioning (ISHVAC), Jinan, China, 19–22 October 2017; pp. 1927–1933.